Applied Catalysis B: Environmental 337 (2023) 122960

Contents lists available at ScienceDirect

Applied Catalysis B: Environmental

journal homepage: www.elsevier.com/locate/apcatb

TiN anchored mesoporous single-crystalline $LaTiO_2N$ with ohmic contact to expedite photocarrier separation for efficient photocatalytic water splitting

Lina Wang [a,b,1], Jinxing Yu [a,1], Zhuo Li [c], Xiaoxiang Xu [a,b,*]

[a] Clinical and Central Lab, Putuo People's Hospital, Tongji University, Shanghai 200060, China
[b] Shanghai Key Lab of Chemical Assessment and Sustainability, School of Chemical Science and Engineering, Tongji University, Shanghai 200092, China
[c] College of Environment Science and Engineering, Tongji University, Shanghai 200092, China

ARTICLE INFO

Keywords:
Schottky interface
Ohmic interface
Mesoporous single crystal
TiN
Photocatalyst
$LaTiO_2N$
Water splitting

ABSTRACT

$LaTiO_2N$ is a promising photocatalyst for solar water splitting but is generally subject to a low activity due to inadequate separation of photocarriers (i.e. e^- and h^+). Loading noble metal cocatalysts such as Pt often has limited improvements because of their Schottky-type interfaces with $LaTiO_2N$, resulting in a deficient electron collection at the surface catalytic sites. In this work, TiN nanoparticles have been firmly anchored at the surface of mesoporous single-crystalline $LaTiO_2N$. As opposed to Pt, TiN has an ohmic contact with $LaTiO_2N$ due to a comparable work function and the structurally matched heterointerfaces. Such a tight and ohmic connection enables TiN to readily collect electrons from $LaTiO_2N$, which in turn substantially improves the photocarrier separation and photocatalytic activity. These findings justify that TiN is an ideal relay for electron transfer between n-type semiconductors and noble metal cocatalysts which would otherwise be very difficult when the Schottky-type interfaces are formed.

1. Introduction

With the solar insolation as the only energy input, photocatalytic water splitting offers a technically simple and environmentally benign means to generate hydrogen fuel, the ideal energy resource for the future [1–6]. Despite the fact that overall water splitting has been efficiently realized in some wide-bandgap semiconductors irradiated by UV light [7–10], it is rather difficult to do so using narrow-bandgap semiconductors that can harvest a large bandwidth of the solar spectrum [11–15]. In general, there is a tradeoff between the light absorption of a semiconductor and its photocarrier energetics [16–19]. How to promote transportation/transfer of low energetic photocarriers is a critical issue to be addressed in order to realize efficient water splitting reactions over narrow-bandgap semiconductors.

Among various narrow-bandgap semiconductors reported, perovskite oxynitrides $AM(O, N)_3$ (A = Ca, Sr, Ba, La; M = Ti, Nb and Ta) have garnered much attention, not only due to their intense visible light absorption but also because of their proper band edge positions that straddle the water redox potential [20–27]. Notably, $LaTiO_2N$ owns an absorption edge as far as 600 nm and comprises mostly earth abundant elements, being of great potential for scalable solar water splitting [28,29]. Notwithstanding these desirable properties, $LaTiO_2N$ normally shows a relatively low photocatalytic activity even under the assistance of a cocatalyst and a sacrificial agent [30,31]. As synthesis of $LaTiO_2N$ generally involves the high-temperature annealing under a non-equilibrium flowing ammonium atmosphere [32–36], the product often intrinsically contains a high concentration of defects (Ti^{3+}, oxygen/nitrogen vacancies, etc.) which severely trap photocarriers and mediate their recombination. In particular, photo-generated electrons are found to be accumulated at deep-level defect states in $LaTiO_2N$ and are hardly accessible to the Pt cocatalyst for water-reduction reactions [37,38]. This is at least partially attributed to the high work function of Pt (> 5.5 eV) that tends to form the Schottky-type interfaces with $LaTiO_2N$ [39–41], preventing efficient electron transfer from $LaTiO_2N$ to Pt. These spatially confined electrons greatly increase the risk of photocarrier recombination and substantially undermine the photocatalytic activity especially for H_2-evolution [38]. Furthermore, the situation become even worse when $LaTiO_2N$ powders contain large amounts of grain boundaries. These grain boundaries can efficiently intercept intergranular photocarrier transportation [20,42], being likely another reason for the poor activity. From these considerations, strategies to enhance electron collection at the surface as well as to reduce the grain

* Corresponding author at: Clinical and Central Lab, Putuo People's Hospital, Tongji University, Shanghai 200060, China.
E-mail address: xxxu@tongji.edu.cn (X. Xu).
[1] These authors contributed equally to this work.

https://doi.org/10.1016/j.apcatb.2023.122960
Received 19 May 2023; Received in revised form 3 June 2023; Accepted 4 June 2023
Available online 5 June 2023

boundaries would be highly useful to upgrade the photocatalytic level of $LaTiO_2N$.

Titanium nitride (TiN), a metallic ceramic material, has recently been found to be a good additive to improve the photocatalytic activity of various semiconductors [43–49]. Such improvements are generally attributed to the plasmonic properties of TiN that are similar to metallic gold and silver nanoparticles [50,51]. Apart from plasmonic properties, TiN is characterized by a small work function (~ 4.2 eV) [49,52], potentially being a good electron collector for a wealth of n-type semiconductors. For instance, TiN forms a purely ohmic junction with anatase TiO_2, enabling efficient electron collection [49]. Since $LaTiO_2N$ shares a similar work function with anatase TiO_2 [53–55], it is a reasonable strategy to enhance the electron collection of $LaTiO_2N$ by introducing TiN. One the other hand, mesoporous single crystals (MSCs) are known to be highly porous and free of grain boundaries, favoring charge migration from bulk to the surface [20,24,56,57]. Their large inner surface and structurally coherent skeletons render MSCs a good platform for electron collection. Combining these considerations, it is of great promise to improve the activity level of $LaTiO_2N$ by constituting heterostructures between TiN and $LaTiO_2N$ MSCs.

In this work, TiN nanoparticles anchored $LaTiO_2N$ MSCs, i.e. TiN@$LaTiO_2N$, were successfully prepared by a one-step synthetic route that topotactically converts $Bi_2La_2Ti_3O_{12}$ via high-temperature ammonolysis. The TiN nanoparticles are found to be strongly interacted with $LaTiO_2N$ MSCs because of their structurally matched heterointerfaces. Such intimate and ohmic connection allows TiN to efficiently collect electrons from $LaTiO_2N$ MSCs thereby spatially separating the photocarriers. The usefulness of TiN is also reflected by the much improved photocatalytic activity of TiN@$LaTiO_2N$ for both water splitting half-reactions and Z-scheme overall water splitting.

2. Experimental

2.1. Material synthesis

TiN anchored $LaTiO_2N$ MSCs, i.e. TiN@$LaTiO_2N$ were prepared by high-temperature ammonolysis using $Bi_2La_2Ti_3O_{12}$ as the precursor. The precursor $Bi_2La_2Ti_3O_{12}$ was synthesized by a molten salt flux method: briefly, 0.3259 g La_2O_3 (Aladdin, 99.9%), 0.2396 g TiO_2 (Jianghu Chemical), 0.4664 g Bi_2O_3 (Aladdin 99.9%), 2.9279 g NaCl (Aladdin 99.9%), and 3.7463 g KCl (Aladdin 99.9%) were thoroughly blended using an agate mortar and a pestle. These powders were pretreated in a muffle furnace at 350 °C (for La_2O_3 at 700 °C) for 2 h prior to weighing to remove moisture absorbed. The mixtures were subsequently annealed at 900 °C for 12 h in the furnace and cooled to room temperature naturally. Afterwards, the product powders were rinsed thoroughly with distilled water and were desiccated at 80 °C. The resultant powders were identified to be $Bi_2La_2Ti_3O_{12}$ by XRD analysis and were used subsequently for high-temperature ammonolysis. The high-temperature ammonolysis was performed in a tube furnace at 900 °C for 8 h. Ultrapure ammonia gas (Jiaya Chemicals, 99.999%) was directed into the tube furnace at a constant flow rate of 200 mL/min. After naturally cooling the furnace to room temperature, the product powders were rinsed with distilled water and were dried at 80 °C overnight.

For comparison purposes, pristine $LaTiO_2N$ and TiN powders were also prepared under the same setup. The $LaTiO_2N$ was prepared using $La_2Ti_2O_7$ as the precursor which was obtained according to a previous report [58]. The TiN was prepared using commercial P25 (Jianghu Chemical) as the precursor. The ammonolysis conditions were used as the same with TiN@$LaTiO_2N$. Physical mixtures of $LaTiO_2N$ and TiN powders were obtained by mechanical grinding their powders at a molar ratio of 2:1. The mixtures were denoted as TiN-$LaTiO_2N$ for clarity.

2.2. Materials characterizations

The as-prepared sample powders were analyzed by X-ray powder diffraction (XRD) analysis using a Bruker D8 Focus diffractometer (Bruker, Germany). Incident radiation used was Cu $K_{\alpha1}$ ($\lambda = 1.5406$ Å) and Cu $K_{\alpha2}$ ($\lambda = 1.5444$ Å). UV-Visible diffuse reflectance spectroscopy (UV–vis DRS) of sample powders were collected on a JASCO V-750 spectrophotometer. The reference non-absorbing material was $BaSO_4$. A field emission scanning electron microscope (JSM-7900 F) and a transmission electron microscope (JEOL JEM-2100) were used to inspect the microstructures of sample powders. The surface chemical states were probed by X-ray photoelectron spectroscopy (XPS) on Thermo Escalab 250 with a monochromatic Al K_α source. The XPS data were calibrated by referring to the adventitious carbon C 1 *s* peak at 284.7 eV. XPS PEAKFIT software was used to fit the XPS data. Gaussian-Lorentzian functions (20% Lorentzian weighting) were adopted for peak fit and the background was assumed to be Shirley-type. Surface areas of sample powders were assessed using a Micromeritics instrument TriStar 3000 and were determined based on the Brunauer-Emmett-Teller (BET) model. Photoluminescence (PL) spectra were collected by a fluorescence spectrophotometer (F-700, Hitachi, Japan) with an excitation photon wavelength of 400 nm. Time-resolved PL decay spectra were collected on a spectrophotometer (FL-1016, Horiba, Japan). The excitation source is a 340 nm nanosecond pulse laser and data were acquired at PL peak position. Current-voltage (*I-V*) curves were collected on a Zahner electrochemical workstation using the sample pellet at a two-electrode setup. The pellet was obtained by uniaxially pressing 150 mg sample powders at 5 MPa. The sample pellet typically has a diameter of 5 mm and a thickness of 2.5 mm, and was sandwiched with two Pt electrodes for *I-V* measurements at room temperature.

2.3. Photocatalytic properties

The photocatalytic performance of sample powders was tested according to their H_2- and O_2-evolution from water under visible light illumination ($\lambda \geq 420$ nm). The experiments were performed in a gas-tight photocatalytic testing system (Perfect Light Labsolar 6 A) with a top-irradiation type reactor. The temperature of the reactor was maintained at 8 °C using a water jacket. The sample powders were deposited with Pt or CoO_x as a cocatalyst according to previous reports [59–62]. Silver nitrate and sodium sulfite was adopted as the sacrificial agent to promote water oxidation and reduction reactions, respectively. In a typical experiment, 100 mg CoO_x-loaded powdery sample and 200 mg La_2O_3 were dispersed into $AgNO_3$ aqueous solution (100 mL, 0.05 M). The La_2O_3 was used as a buffer to control the pH of the solution at ca. 8.5. The resultant suspensions were evacuated for 60 min to remove air dissolved. Visible light was generated using a 300 W Xeon lamp (Perfect Light, PLX-SXE300) coupled with an UV cutoff filter ($\lambda \geq 420$ nm). The gas component within the reactor was analyzed by an online gas chromatography (GC2014C, SHIMADZU, Japan). The apparent quantum efficiency (AQE) was determined under the same setup. Monochromatic light source was produced by filtering the output of a 300 W Xenon lamp with a band-pass filter at 420 nm, 450 nm, 500 nm, 550 nm and 600 nm, respectively. The photon flux at each wavelength was calibrated using a quantum meter (Apogee MP-300, USA). The AQE for O_2 and H_2 production was then determined according to the following equation (Eq. 1):

$$AQE = \frac{n \times \text{mol of gas production per } hour}{\text{mol of photon flux per } hour} \times 100\% \quad (1)$$

where n = 4 for O_2 and n = 2 for H_2.

The Z-scheme overall water splitting experiment was performed in the same setup. Specifically, 50 mg CoO_x-loaded (1 wt%) TiN@$LaTiO_2N$ were mixed up with 50 mg Ru-loaded (0.5 wt%) $SrTiO_3$ doped with Rh ($SrTiO_3$:Rh). The Ru-loaded $SrTiO_3$:Rh powders were prepared following a previous report [63]. The mixtures were dispersed into 100 mL $FeCl_3$ aqueous solution (2 mM) whose pH was controlled by hydrochloric acid at ca. 2.5.

2.4. Theoretical calculation and simulation

The theoretical calculations were performed based on density functional theory (DFT) using commercial Vienna ab-initio simulation package (VASP). The Perdew-Burke-Ernzerhof (PBE) functional with the generalized gradient approximation (GGA) was implemented during calculation. The projector augmented wave (PAW) method was adopted to describe the valence electron configurations. The plane-wave cutoff was 450 eV. TiN (001) facets and $LaTiO_2N$ (101) facets were constructed for DFT calculation. Both types of facets comprise at least five atom layers with a vacuum distance of 20 Å at the top. All structures were fully relaxed to reduce the force on each atom (< 0.02 eV/Å). The convergence criterion was set to be 10^{-5} eV. A Monkhorst-Pack k-points mesh of 6 × 6 × 1 was sampled for TiN (001) facets and $LaTiO_2N$ (101) facets.

The photocarrier distribution within $LaTiO_2N$ semiconductor was simulated using the semiconductor module of COMSOL Multiphysics software following the same method in the literature [64,65]. Semiconductor parameters of $LaTiO_2N$ were collected from the literature and were listed in Table S1. A two-dimensional (2D) model was adopted to simplify the simulation. Generation of photocarriers was assumed to be uniform due to the light reflection and scattering in powdery sample. A high defect concentration (2×10^{18} cm^{-3}) was used for $LaTiO_2N$ and the photocarrier recombination was set to be Shockley-Reed-Hall type. The interface was assumed to be Schottky-type for $LaTiO_2N$|electrolyte and $LaTiO_2N$|Pt but to be ohmic for $LaTiO_2N$|TiN.

3. Results and discussion

3.1. Crystal structure and microstructures

TiN anchored $LaTiO_2N$ MSCs, i.e. TiN@$LaTiO_2N$, have been prepared readily by one step ammonolysis treatment of $Bi_2La_2Ti_3O_{12}$ at high temperatures. As a precursor, the $Bi_2La_2Ti_3O_{12}$ is an Aurivillius compound [66], comprising alternate stacking of $[Bi_2O_2]^{2+}$ unit and $[La_2Ti_3O_{10}]^{2-}$ perovskite block (Fig. 1a). The high geometric similarity of perovskite blocks in $Bi_2La_2Ti_3O_{12}$ and $LaTiO_2N$ suggests that $Bi_2La_2Ti_3O_{12}$ can be topotactically transformed into $LaTiO_2N$ without substantial atom migration and rearrangements. This is evidently shown by their field emission scanning electron microscopic (FE-SEM) images (Fig. 1c-d). The plate-like morphologies of $Bi_2La_2Ti_3O_{12}$ particles are well-preserved in the product particles except that the latter has a high porosity. Rietveld refinements suggest that the product contains $LaTiO_2N$ and TiN phases in a molar ratio of 2:1. The Bi^{3+} cations are known to be reduced into element Bi during high-temperature ammonolysis and become quite volatile thereby can be quickly removed from the system[20,24,56,57]. The reaction formula can then be written as follows (Eq. 2):

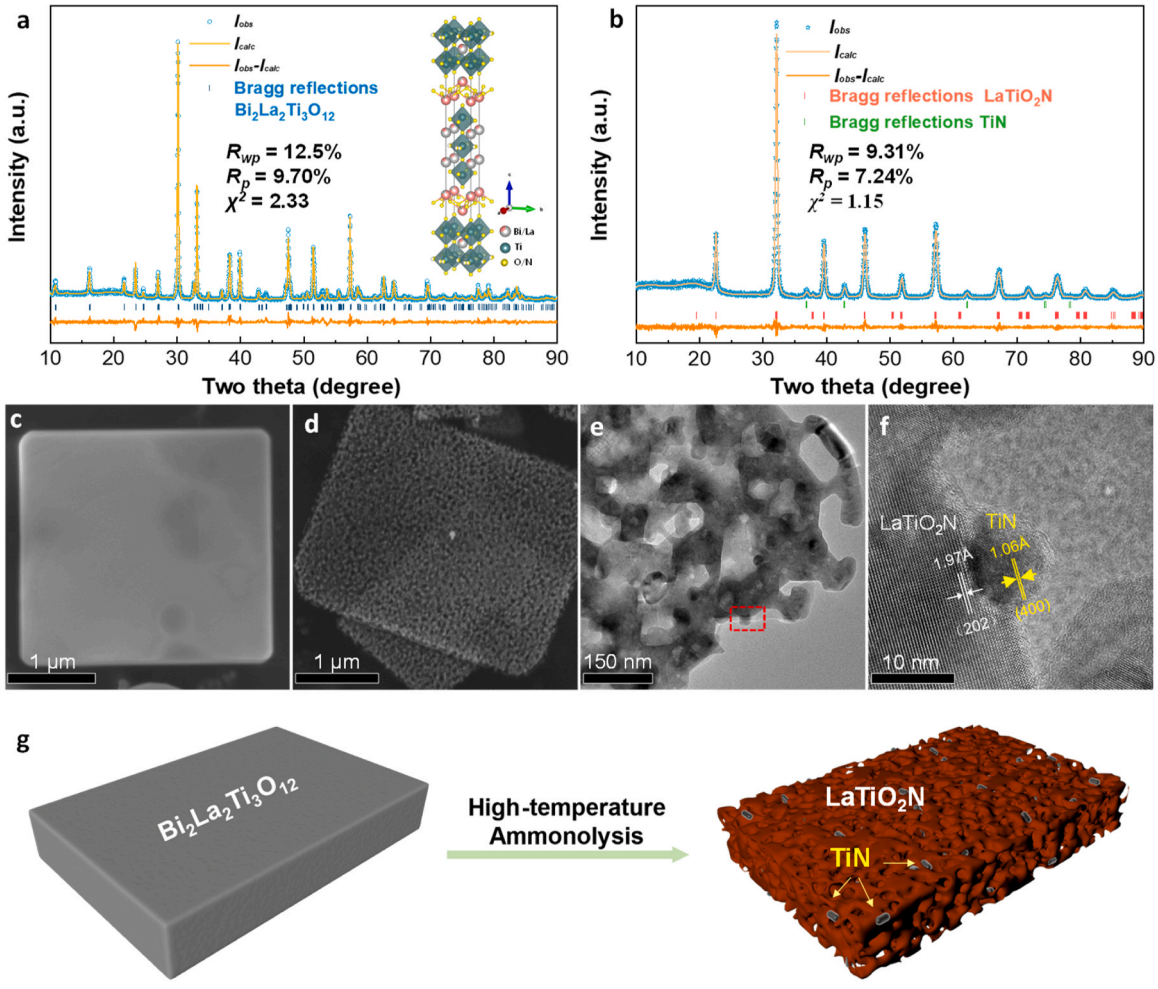

Fig. 1. Structural and microstructural analysis: (a) Rietveld refinement of XRD patterns of $Bi_2La_2Ti_3O_{12}$ precursor, its refined crystal structure and agreement factors are shown as insets; (b) Rietveld refinement of XRD patterns of TiN@$LaTiO_2N$, the agreement factors are inserted as insets; (c) FE-SEM image of $Bi_2La_2Ti_3O_{12}$ precursor; (d) FE-SEM image of TiN@$LaTiO_2N$; (e) TEM image of TiN@$LaTiO_2N$; (f) high-resolution TEM image of region marked by red rectangle of (e), lattice fringes marked correspond to (202) plane of $LaTiO_2N$ and (400) plane of TiN; (g) schematic illustration of synthetic process from $Bi_2La_2Ti_3O_{12}$ to TiN@$LaTiO_2N$ via high-temperature ammonolysis.

$$6Bi_2La_2Ti_3O_{12} + 32NH_3 \rightarrow 12LaTiO_2N + 6TiN + 48H_2O + 12Bi^{\uparrow} + 7N_2^{\uparrow} \quad (2)$$

Although the product contains two phases, EDS mapping analysis suggests uniform distribution of all constituent elements over a single plate-like particle of TiN@$LaTiO_2N$ (Fig. S1). FE-SEM and TEM analysis further reveals that the particle not only comprises the three-dimensional porous $LaTiO_2N$ skeletons but also has copious nanosized TiN granules that are tightly and homogeneously anchored at the skeleton surface (Fig. 1e-f, Fig. S2). The porous $LaTiO_2N$ skeletons are essentially of single crystallinity according to the sharp and coherent selected area diffraction (SAED) patterns (Fig. S3). The $LaTiO_2N$ skeletons are found to be oriented along [010] zone axis, being in a good agreement with the topotactic transformation mechanism from $Bi_2La_2Ti_3O_{12}$ to $LaTiO_2N$. The strong adherence between TiN and $LaTiO_2N$ is revealed by their interfaces according to the high-resolution TEM image (Fig. 2). The interfaces are formed by TiN (100) and $LaTiO_2N$ (101) facets which are seamlessly attached to each other. This phenomenon can be rationalized by their comparable atomic arrangements and lattice *d*-spacing that help to reduce the surface energy [67–69]. Such peculiar microstructures are distinct from pristine TiN, $LaTiO_2N$, and their mixtures TiN-$LaTiO_2N$ (Fig. S4). For instance, pristine $LaTiO_2N$ comprises irregular-shaped particles containing copious grain boundaries and TiN-$LaTiO_2N$ involves randomly and loosely compacted TiN and $LaTiO_2N$ particles. This is also properly reflected from BET surface analysis and pore size distribution (Fig. S5). Thereby, through one-step ammonolysis of $Bi_2La_2Ti_3O_{12}$, TiN anchored $LaTiO_2N$ MSCs can be facile prepared.

3.2. Photocatalytic water splitting

The photocatalytic behavior of different sample powders was then studied by comparing their activities in water splitting half reactions. Blank control experiments in the absence of catalyst or light were examined first to secure gas evolution origins from photocatalytic processes. Fig. 3a illustrates the typical O_2-evolution profiles of different samples illuminated by visible light ($\lambda \geq 420$ nm). Although all samples were photo-deposited with the same amounts of cocatalyst CoO_x (1 wt %), they deliver distinct activities for water oxidation into O_2. Pristine $LaTiO_2N$ shows only mild activity for O_2-evolution, being consistent with the results reported in the literature for untreated $LaTiO_2N$ [31]. TiN, albeit being inactive for O_2-evolution alone, can clearly improve the performance of $LaTiO_2N$ by a factor of ~ 2 through physical mixing. More interestingly, much more improved activity (by a factor of 13) is observed for TiN@$LaTiO_2N$ in which TiN is intimately anchored at the surface of $LaTiO_2N$. This trend is more pronounced in water reduction reactions (Fig. 3b). Pristine $LaTiO_2N$ is typically inert for H_2-evolution which has been ascribed to a poor transfer of electrons from $LaTiO_2N$ to Pt cocatalyst [37,38]. The presence of TiN, however, can clearly activate $LaTiO_2N$ for H_2-evolution, particularly when they are strongly bound to $LaTiO_2N$. Previous studies suggest that TiN can be a plasmonic material to inject hot electrons to semiconductors in the range from visible to infrared light [49,50]. Nevertheless, plasmonic properties of TiN may not play a primary role here as the action spectra of TiN@$LaTiO_2N$ follow the light absorption curve of $LaTiO_2N$ rather than that of TiN (Fig. 3c and Fig. S6). For instance, no O_2- and H_2-evolution was detected above 600 nm which is close to the light absorption threshold of $LaTiO_2N$. After proper optimization of CoO_x content and synthetic temperature (Fig. S7), the TiN@$LaTiO_2N$ delivers an apparent quantum efficiency (AQE) as high as ~ 17% for O_2-evolution. The data for AQE determination were tabulated in Table S5. The AQE values are quite high among the literature [29,31,70–73] as no additional treatment, e.g. air annealing or acid etching [29,74], was applied to $LaTiO_2N$. It is worth noting that TiN@$LaTiO_2N$ owns a much better activity for O_2-evolution than for H_2-evolution and fails to photocatalyze overall water splitting. This is probably due to the severe trapping of photo-generated electrons by deep-level defect states of $LaTiO_2N$ that inhibit water reduction reactions [37]. Nevertheless, O_2-evolution half-reactions have been considered to be the rate limiting steps for overall water splitting reactions. The high activity of TiN@$LaTiO_2N$ for O_2-evolution is therefore very useful for the Z-scheme type overall water splitting. As an exemplification, a Z-scheme system comprising TiN@$LaTiO_2N$, $SrTiO_3$:Rh, and Fe^{2+}/Fe^{3+} redox couple was built which showed stable activity in splitting water into stoichiometric H_2 and O_2 under visible light illumination (Fig. 3d).

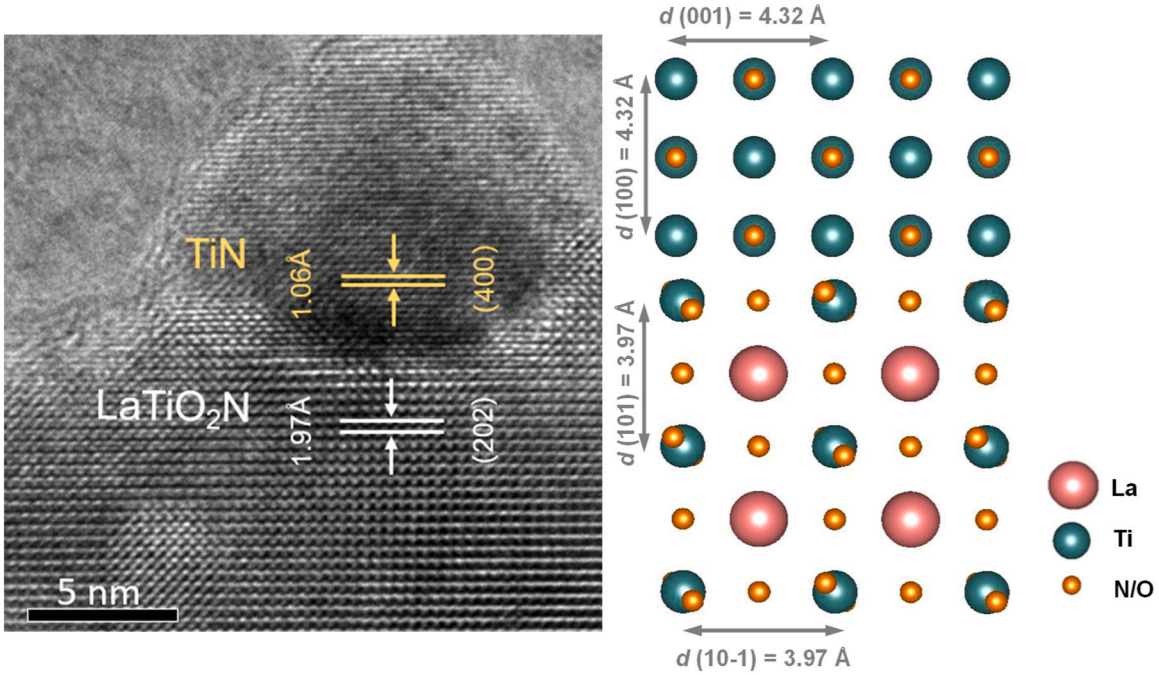

Fig. 2. High resolution TEM image at the interface of TiN@$LaTiO_2N$ (left), schematic illustration of crystal structure at the interface (right); the interface can be formed due to a similar *d*-spacing between TiN (001) plane (4.32 Å) and $LaTiO_2N$ (101) plane (3.97 Å).

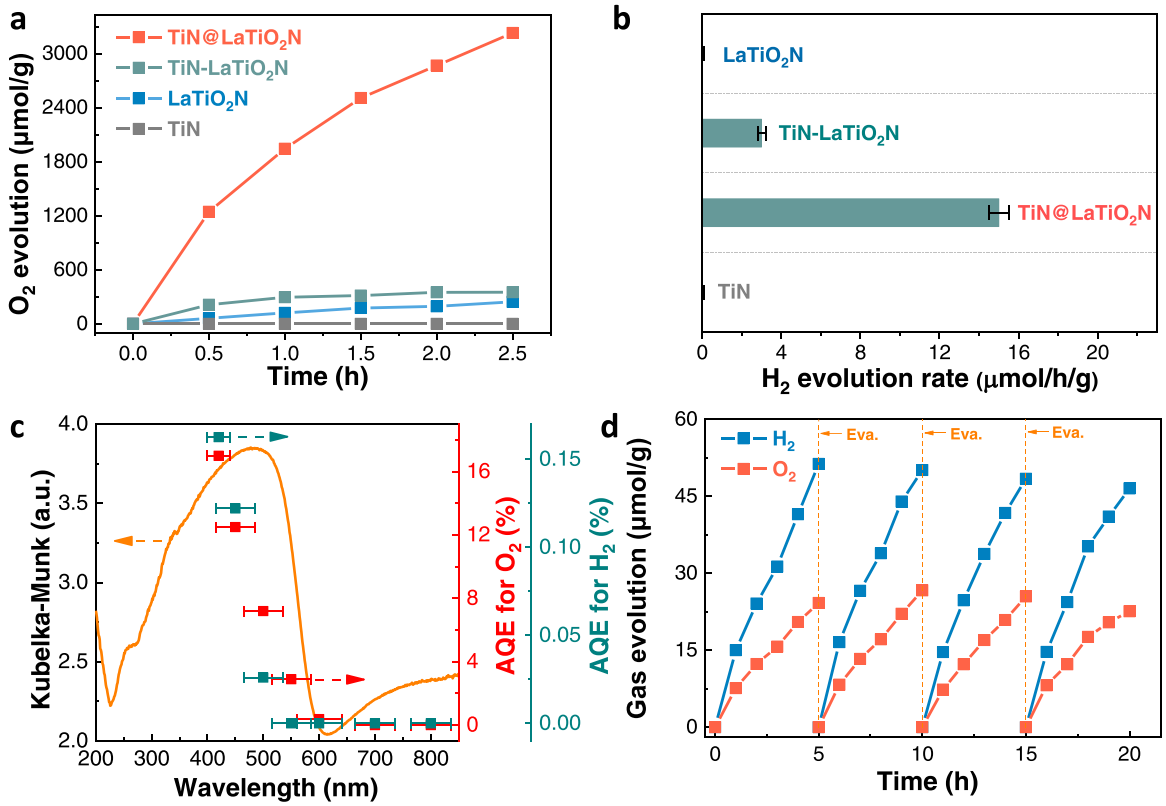

Fig. 3. Photocatalytic performance: (a) O_2-evolution profiles of TiN, TiN@$LaTiO_2N$, TiN-$LaTiO_2N$, and $LaTiO_2N$ under visible light illumination ($\lambda \geq 420$ nm), silver nitrate (0.05 M) was used as the sacrificial agent; (b) H_2-evolution rates of TiN, TiN@$LaTiO_2N$, TiN-$LaTiO_2N$, and $LaTiO_2N$ under visible light illumination ($\lambda \geq 420$ nm), sodium sulfite (0.05 M) was used as the sacrificial agent; (c) action spectra of TiN@$LaTiO_2N$ for O_2- and H_2-evolution; (d) Z-scheme overall water splitting over TiN@$LaTiO_2N$ loaded with 1 wt% CoO_x (50 mg), $SrTiO_3$:Rh loaded with 0.5 wt% Ru (50 mg), Fe^{2+}/Fe^{3+} redox couple (0.002 M), evacuation was performed every 5 h.

3.3. XPS and PL spectroscopy

Given the large dissimilar activities among samples, we sought to explore the role of TiN on the modification of $LaTiO_2N$. First, XPS spectra of TiN, TiN-$LaTiO_2N$, TiN@$LaTiO_2N$, and $LaTiO_2N$ were collected to study their surface states. Fig. 4a shows the Ti 2*p* state of these samples. The Ti 2*p* state of pristine $LaTiO_2N$ is characterized by two spin-orbit doublets assignable to Ti^{4+} and Ti^{3+} species. These signals are typically seen in as-prepared $LaTiO_2N$ without further treatment, indicating that $LaTiO_2N$ is indeed rich in defects. The TiN, however, shows an additional spin-orbit doublet at low binding energy side. This new doublet is probably due to Ti^{3+} species coordinated to N^{3-} anions[75]. For TiN-$LaTiO_2N$ and TiN@$LaTiO_2N$, their Ti 2*p* states can be properly unfolded into five spin-orbit doublets, considering the contribution from both $LaTiO_2N$ and TiN (see Table S2-S3). Compared with pristine $LaTiO_2N$ and TiN, TiN@$LaTiO_2N$ has clear shifts in the binding energy of all signals, as opposed to TiN-$LaTiO_2N$ which shows almost no shift. More specifically, for TiN@$LaTiO_2N$, signals belong to $LaTiO_2N$ are shifted to higher binding energy while those of TiN shows an opposite trend. Similar observations were also noticed in the O 1*s* state in which TiN@$LaTiO_2N$ has a much larger shift than TiN-$LaTiO_2N$. These differences can be ascribed to the strong interactions between $LaTiO_2N$ and TiN in the sample of TiN@$LaTiO_2N$. Strong interactions are known to be beneficial for charge migration and separation, as further confirmed by the PL spectra and time-resolved PL (TRPL) decay profiles. The PL spectra of pristine $LaTiO_2N$ under bandgap excitation involve a broad peak centered at ~ 600 nm (Fig. 4c). This peak can be assigned to band-edge emission of $LaTiO_2N$ whose intensity is considerably decreased in the presence of TiN. In addition, TRPL decay profiles show that TiN at least doubles the decay lifetime of band-edge emission of $LaTiO_2N$, indicating that TiN helps to increase the long-lived photocarriers. Combining these results, one can readily realize that TiN can substantially improve the photocarrier separation conditions in $LaTiO_2N$, particularly when they are intimately connected.

3.4. Photocarrier separation

To further investigate the photocarrier separation in TiN@$LaTiO_2N$, we have carried out a Pt photo-deposition experiment as the chemical probe to identify the position of photo-generated electrons [76]. Fig. 5a illustrates a dark field TEM image of TiN@$LaTiO_2N$ which has been illuminated in the presence of H_2PtCl_6 aqueous solution (0.01 M) for 30 min. As revealed by selected area EDS analysis (Fig. 5b), the photo-deposited Pt nanoparticles are mostly located on TiN rather than on $LaTiO_2N$. In addition, illuminating pristine TiN alone under the same conditions results in no discernable Pt deposition (Fig. S8). These results jointly suggest that TiN can accept photo-generated electrons from $LaTiO_2N$ and plasmonic effect of TiN does not play an important role here. Previous investigations suggest that noble metal cocatalyst Pt can hardly accept electrons from $LaTiO_2N$, being one of the major reasons for the poor photo-reduction activity of $LaTiO_2N$ [37,38]. In this regard, the good electron-accepting property of TiN provides a tangible means to circumvent this problem and well-explains the improved H_2-evolution performance of TiN@$LaTiO_2N$. The facile electron transfer from $LaTiO_2N$ to TiN also implicates that photocarrier separation conditions are improved as electrons and holes can be spatially segregated.

An intuitive question arises as why TiN can readily accept electrons from $LaTiO_2N$ but Pt cannot. To address this question, we have carried out DFT calculations on the interfacial properties of TiN@$LaTiO_2N$ based on the structure model revealed by TEM analysis. Fig. 6a-b

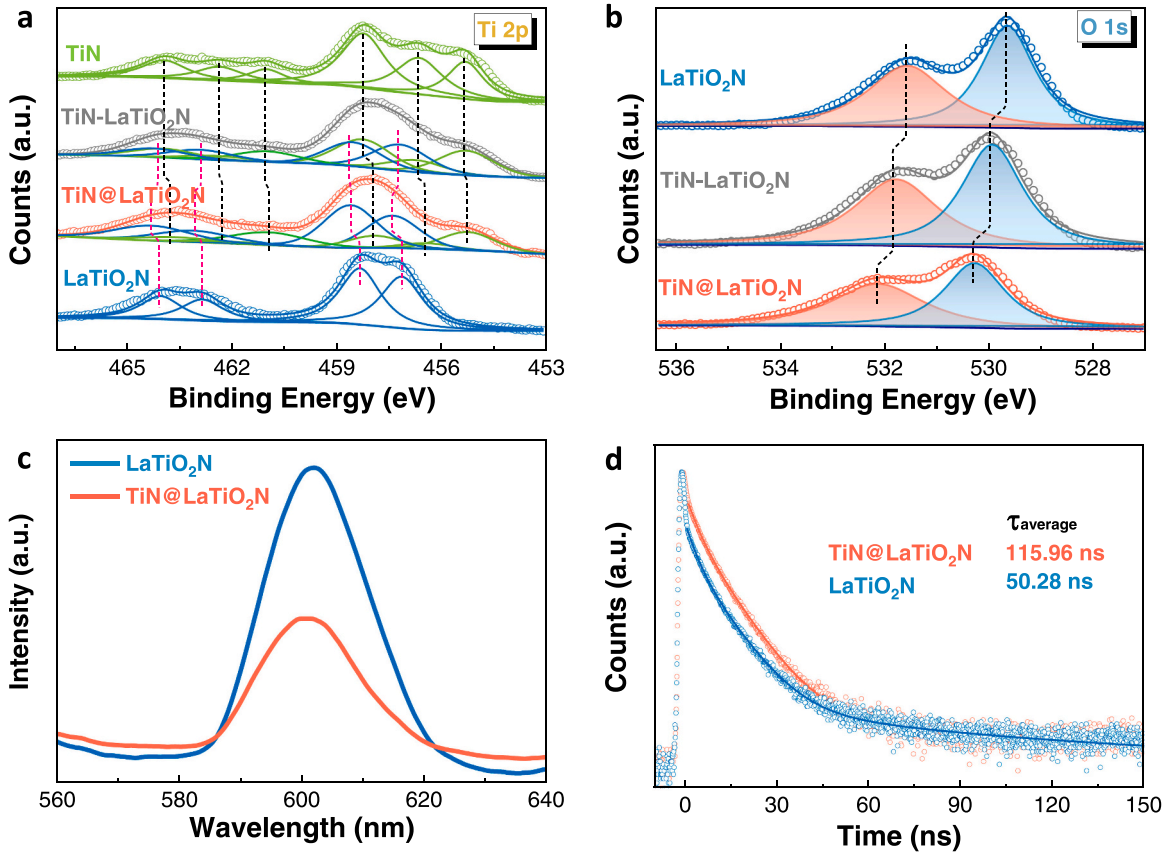

Fig. 4. XPS spectra of TiN, TiN-$LaTiO_2N$, TiN@$LaTiO_2N$, $LaTiO_2N$: (a) Ti 2*p* state; (b) O 1 *s* state; (c) photoluminescence (PL) spectra of $LaTiO_2N$ and TiN@$LaTiO_2N$; (d) time-resolved PL decay profiles of $LaTiO_2N$ and TiN@$LaTiO_2N$, amplitude-weighted average decay lifetime is shown as insets.

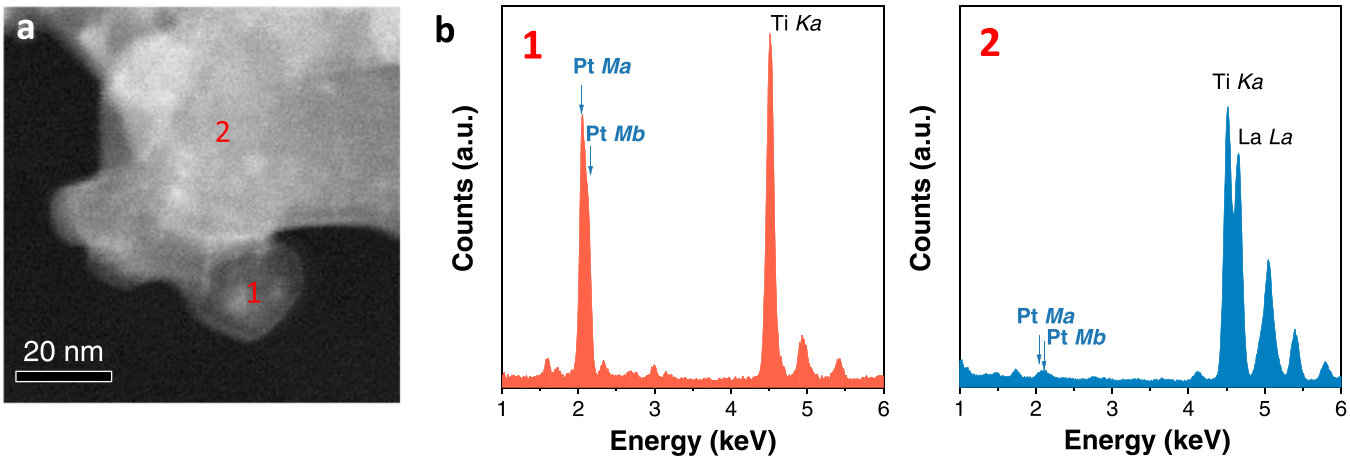

Fig. 5. (a) Dark field TEM image of TiN@$LaTiO_2N$; (b) EDS spectra at selected points marked in (a).

illustrates the calculated work function of TiN (001) surface and $LaTiO_2N$ (101) facets. A similar work function (~ 3.5 eV) can be noticed for these two facets, implying that there is almost no potential barrier for electron transfer across the interface formed by TiN (001) and $LaTiO_2N$ (101) facets, i.e. an ohmic-type behavior. However, this is not the case for Pt which is known to have a high work function (> 5.5 eV). Consequently, the interface between $LaTiO_2N$ and Pt is essentially a Schottky-type one and is characterized by a high energy barrier for the interfacial electron transfer. These deductions are further verified by the current-voltage (*I-V*) behavior of the symmetric cells with $LaTiO_2N$|Pt and $LaTiO_2N$|TiN|Pt interfaces, as illustrated in Fig. 7a-b. For the $LaTiO_2N$|Pt symmetric cell (Fig. 8a), the *I-V* curve shows a typical current rectification, being expected for the Schottky-type interface (Fig. 7c). In contrast, the $LaTiO_2N$|TiN|Pt symmetric cell exhibits an almost linear *I-V* relation in the same voltage range, indicative of the ohmic interface (Fig. 7d). These distinct *I-V* behaviors evidently suggest that TiN can facilely collect electrons from $LaTiO_2N$ and serves as an electron relay between $LaTiO_2N$ and Pt. Moreover, DFT calculations reveal a strong interplay when TiN (001) facet is attached to $LaTiO_2N$ (101) facet. Specifically, atoms at the interface undergo severe electron depletion and accumulation phenomena (Fig. 6c), suggesting that chemical bonds are formed at interfacial atoms. These chemical bonds are potential

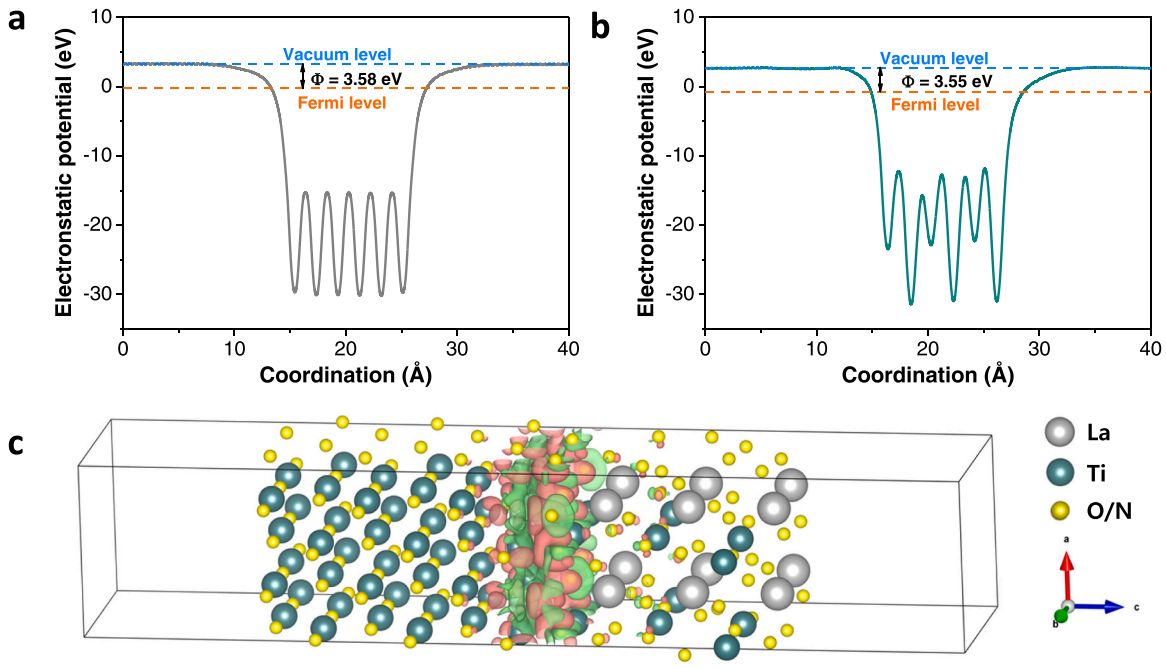

Fig. 6. (a) The calculated work function of TiN (001) surface; (b) the calculated work function of $LaTiO_2N$ (101) surface; (c) charge density difference at the heterointerface between TiN (001) and $LaTiO_2N$ (101) surface, electron depletion and accumulation is indicated by green and red color, respectively.

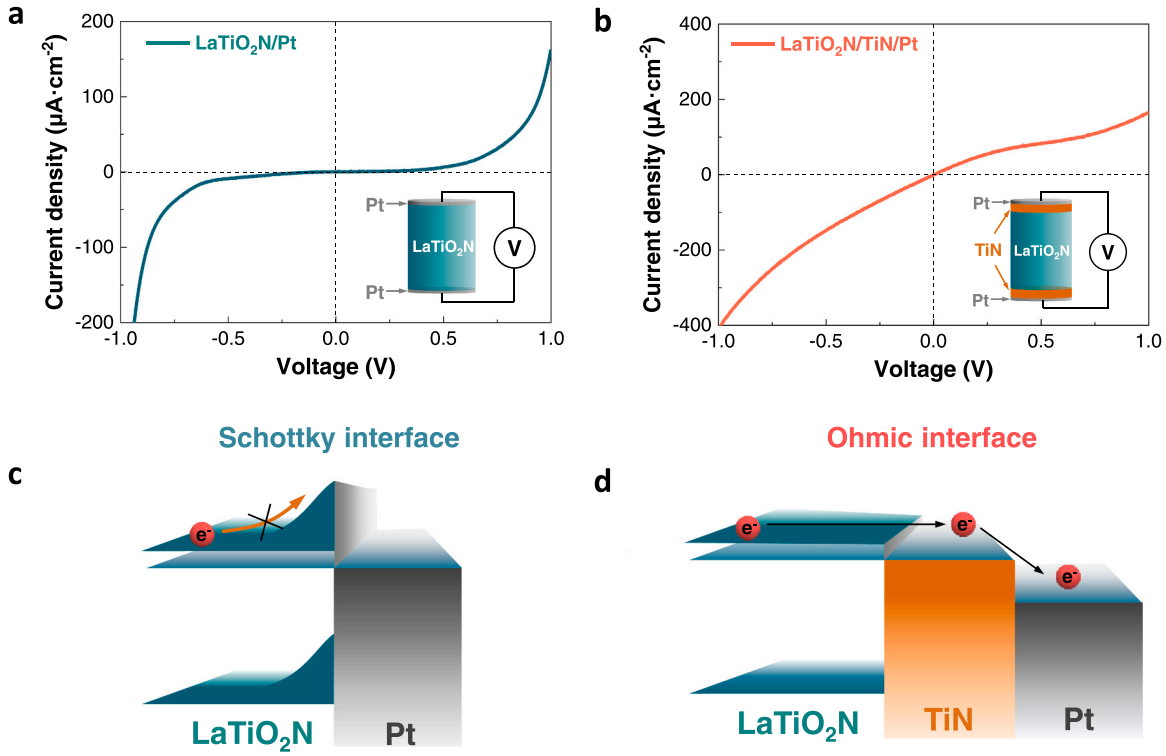

Fig. 7. (a) Current-voltage (*I-V*) curve of a $LaTiO_2N$/Pt symmetric cell; (b) *I-V* curve of a $LaTiO_2N$/TiN/Pt symmetric cell, the cell configurations are shown as the insets; (c) band diagram of $LaTiO_2N$ in contact with Pt, representing a Schottky interface; (d) band diagram of $LaTiO_2N$ in contact with TiN before connecting to Pt, representing the ohmic interfaces.

channels for charge transportation, endowing TiN@$LaTiO_2N$ a much-improved photocarrier separation condition.

As a direct visualization for the photocarrier separation, we have simulated the photocarrier distribution in $LaTiO_2N$ with and without TiN/Pt attachment under light illumination. The simulation was implemented using the two-dimensional (2D) models based on the geometry of $LaTiO_2N$ MSCs. The interfaces between TiN and $LaTiO_2N$ are set to be ohmic-type while the rest ones are assumed to be Schottky-type as expected for $LaTiO_2N$|electrolyte and $LaTiO_2N$|Pt interfaces. The simulated photocarrier distribution in $LaTiO_2N$, Pt@$LaTiO_2N$, and TiN@$LaTiO_2N$ is illustrated in Fig. 8. As can be seen from Fig. 8a, pristine $LaTiO_2N$ has a much poorer photocarrier separation in the bulk

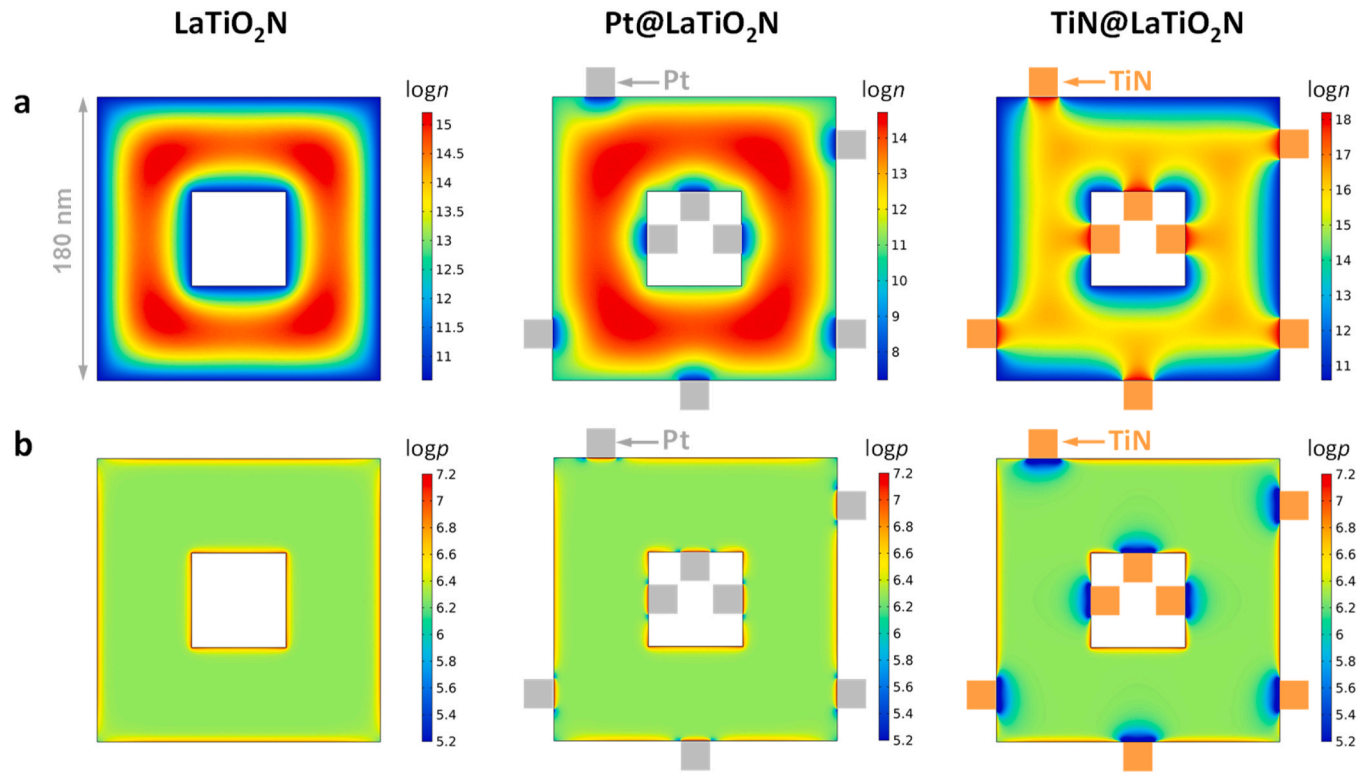

Fig. 8. Simulated photocarrier distribution over 2D models of $LaTiO_2N$, Pt@ $LaTiO_2N$, and TiN@$LaTiO_2N$: (a) photo-generated electrons; (b) photo-generated holes.

than at the surface. In particular, photo-generated electrons are severely confined in the bulk thereby are inaccessible to the surface water-reduction reactions. This situation cannot be changed by anchoring Pt particles which shows no improvement in terms of electron confinement (Fig. 8). Only when TiN particles are attached to $LaTiO_2N$ can these electrons migrate to the surface, demonstrating ameliorated photocarrier separation both in the bulk and at the surface. These results consistently reveal the important role of TiN in expediting photocarrier separation in $LaTiO_2N$ and well-explain the distinct photocatalytic activity observed previously. The unique properties of TiN, e.g. relatively low work function, high electronic conductivity, good chemical stability, etc., indicate that it can be an ideal relay for electron transfer between n-type semiconductors and noble metal cocatalyst (i.e. Pt, Au, Rh, etc.) which would otherwise be rather difficult due to their Schottky-type interfaces. Oxynitrides are typical n-type semiconductor photocatalysts whose photo-generated electrons are normally confined in the bulk of sample particles under water splitting conditions. Loading high work function conductors such as TiN could be an effective way to direct the flow of electrons out of sample particles for water reduction reactions. The TiN particles are preferably loaded by an *in situ* method where matched heterointerfaces can be formed. This work here provides a useful paradigm for the loading TiN particles by using a suitable precursor.

4. Conclusions

Using $Bi_2La_2Ti_3O_{12}$ as the precursor, we have successfully fabricated $LaTiO_2N$ MSCs anchored with TiN nanoparticles (i.e. TiN@$LaTiO_2N$) via a one-step topotactic route. The as-prepared TiN@$LaTiO_2N$ is characterized by a strong interplay between TiN and $LaTiO_2N$ due to the matched heterointerfaces formed by TiN (001) and $LaTiO_2N$ (101) facets. Compared with pristine $LaTiO_2N$ with a poor photocatalytic activity, the TiN@$LaTiO_2N$ demonstrates a much-improved activity for both water oxidation and reduction reactions. For instance, TiN@$LaTiO_2N$ delivers an AQE of ~ 17% at 420 ± 20 nm for O_2-evolution. As opposed to inert $LaTiO_2N$, TiN@$LaTiO_2N$ is also active for water reduction into H_2. DFT calculations suggest a comparable work function for TiN (001) and $LaTiO_2N$ (101) surface and strong chemical interactions at their heterointerfaces. This is also confirmed by current-voltage measurements which reveal an ohmic interface between TiN and $LaTiO_2N$, being distinct to the Schottky-type one between Pt and $LaTiO_2N$. The ohmic contact enables TiN to readily collect photo-generated electrons from $LaTiO_2N$, which in turn ameliorates the photocarrier separation condition of $LaTiO_2N$, as indicated by simulation experiments of photocarrier distribution. The good electron-accepting property renders TiN an ideal relay for electron transfer from n-type semiconductors to noble metal cocatalyst, opening up new possibilities to upgrade the performance of many important photocatalysts.

CRediT authorship contribution statement

Ms. Lina Wang and Mr. Jinxing Yu synthesized the materials and carried out analysis, Prof. Zhuo Li performed the theoretical calculation and Prof. Xiaoxiang Xu administrated the project and did the manuscript writing.

Declaration of Competing Interest

The authors declare no competing interests.

Data Availability

Data will be made available on request.

Acknowledgements

We thank the National Natural Science Foundation of China (Grant No. 51972233, 52172225) and the Fundamental Research Funds for the Central Universities for funding.

Appendix A. Supporting information

Supplementary data associated with this article can be found in the online version at doi:10.1016/j.apcatb.2023.122960.

References

[1] S.S. Chen, T. Takata, K. Domen, Particulate photocatalysts for overall water splitting, Nat. Rev. Mater. 2 (2017) 17050, https://doi.org/10.1038/Natrevmats.2017.50.

[2] X.X. Xu, C. Randorn, P. Efstathiou, J.T.S. Irvine, A red metallic oxide photocatalyst, Nat. Mater. 11 (2012) 595–598. Doi 10.1038/Nmat3312.

[3] G. Zhang, G. Liu, L.Z. Wang, J.T.S. Irvine, Inorganic perovskite photocatalysts for solar energy utilization, Chem. Soc. Rev. 45 (2016) 5951–5984, https://doi.org/10.1039/c5cs00769k.

[4] G.D. Wan, L.C. Yin, X. Chen, X.X. Xu, J. Huang, C. Zhen, H.Z. Zhu, B.H. Huang, W. J. Hu, Z.H. Ren, H. Tian, L.Z. Wang, G. Liu, H.M. Cheng, Photocatalytic overall water splitting over $PbTiO_3$ modulated by oxygen vacancy and ferroelectric polarization, J. Am. Chem. Soc. 144 (2022) 20342–20350, https://doi.org/10.1021/jacs.2c08177.

[5] Y.Y. Kang, H.Z. Qi, G.D. Wan, C. Zhen, X.X. Xu, L.C. Yin, L.Z. Wang, G. Liu, H. M. Cheng, Ferroelectric polarization enabled spatially selective adsorption of redox mediators to promote Z-scheme photocatalytic overall water splitting, Joule 6 (2022) 1876–1886, https://doi.org/10.1016/j.joule.2022.06.017.

[6] H.L. Zhu, C. Zhen, X.T. Chen, S. Feng, B. Li, Y.F. Du, G. Liu, H.M. Cheng, Patterning alternate TiO_2 and Cu_2O strips on a conductive substrate as film photocatalyst for Z-scheme photocatalytic water splitting, Sci. Bull. 67 (2022) 2420–2427, https://doi.org/10.1016/j.scib.2022.11.018.

[7] T. Takata, J.Z. Jiang, Y. Sakata, M. Nakabayashi, N. Shibata, V. Nandal, K. Seki, T. Hisatomi, K. Domen, Photocatalytic water splitting with a quantum efficiency of almost unity, Nature 581 (2020) 411–414.

[8] H. Nishiyama, T. Yamada, M. Nakabayashi, Y. Maehara, M. Yamaguchi, Y. Kuromiya, Y. Nagatsuma, H. Tokudome, S. Akiyama, T. Watanabe, R. Narushima, S. Okunaka, N. Shibata, T. Takata, T. Hisatomi, K. Domen, Photocatalytic solar hydrogen production from water on a 100-m^2 scale, Nature 598 (2021) 304–307, https://doi.org/10.1038/s41586-021-03907-3.

[9] H. Kato, K. Asakura, A. Kudo, Highly efficient water splitting into H_2 and O_2 over lanthanum-doped $NaTaO_3$ photocatalysts with high crystallinity and surface nanostructure, J. Am. Chem. Soc. 125 (2003) 3082–3089. Doi 10.1021/Ja027751g.

[10] Y. Goto, T. Hisatomi, Q. Wang, T. Higashi, K. Ishikiriyama, T. Maeda, Y. Sakata, S. Okunaka, H. Tokudome, M. Katayama, S. Akiyama, H. Nishiyama, Y. Inoue, T. Takewaki, T. Setoyama, T. Minegishi, T. Takata, T. Yamada, K. Domen, A Particulate Photocatalyst Water-Splitting Panel for Large-Scale Solar Hydrogen Generation, Joule 2 (2018) 509–520, https://doi.org/10.1016/j.joule.2017.12.009.

[11] K. Takanabe, Photocatalytic water splitting: quantitative approaches toward photocatalyst by design, ACS Catal. 7 (2017) 8006–8022, https://doi.org/10.1021/acscatal.7b02662.

[12] C.S. Pan, T. Takata, M. Nakabayashi, T. Matsumoto, N. Shibata, Y. Ikuhara, K. Domen, A complex perovskite-type oxynitride: the first photocatalyst for water splitting operable at up to 600 nm, Angew. Chem. Int. Ed. 54 (2015) 2955–2959, https://doi.org/10.1002/anie.201410961.

[13] Y.W. Wang, Y.Y. Kang, H.Z. Zhu, G. Liu, J.T.S. Irvine, X.X. Xu, Perovskite oxynitride solid solutions of $LaTaON_2$-$CaTaO_2N$ with greatly enhanced photogenerated charge separation for solar-driven overall water splitting, Adv. Sci. 8 (2021), 2003343, https://doi.org/10.1002/Advs.202003343.

[14] J.H. Lian, K. Shibata, Y.J. Xiao, S.W. Du, T. Tanaka, Y. Qi, O. Ishitani, K. Maeda, Z. C. Feng, F.X. Zhang, A band-to-band transition visible-light-responsive anatase titania photocatalyst by N,F-codoping for water splitting and CO_2 reduction, J. Mater. Chem. A 11 (2022) 141–148, https://doi.org/10.1039/d2ta08076a.

[15] H. Zou, Y. Qi, S.W. Du, L.F. Liu, X.S. Xin, Y.F. Bao, S.W. Wang, Z.C. Feng, F. X. Zhang, Pyrochlore-structural $Nd_2Ta_2O_5N_2$ photocatalyst with an absorption edge of over 600 nm for Z-scheme overall water splitting, Chem. Commun. 58 (2022) 10719–10722, https://doi.org/10.1039/d2cc02903k.

[16] J.D. Xiao, T. Hisatomi, K. Domen, Narrow-band-gap particulate photocatalysts for one-step- excitation overall water splitting, Acc. Chem. Res. 56 (2023) 878–888, https://doi.org/10.1021/acs.accounts.3c00011.

[17] Y.Q. Xiao, Z.Y. Fan, M. Nakabayashi, Q.Q. Li, L.J. Zhou, Q. Wang, C.L. Li, N. Shibata, K. Domen, Y.B. Li, Decoupling light absorption and carrier transport via heterogeneous doping in Ta_3N_5 thin film photoanode, Nat. Commun. 13 (2023) 7769, https://doi.org/10.1038/s41467-022-35538-1.

[18] S.W. Du, H. Zou, Y.F. Bao, Y. Qi, X.S. Xin, S.W. Wang, Z.C. Feng, F.X. Zhang, Homogeneous nitrogen-doped (111)-type layered $Sr_5Nb_4O_{15-x}N_x$ as a visible-light-responsive photocatalyst for water oxidation, Nano Res. 15 (2022) 9976–9984, https://doi.org/10.1007/s12274-022-4529-6.

[19] Y.F. Bao, C. Li, K. Domen, F.X. Zhang, Strategies and methods of modulating nitrogen-incorporated oxide photocatalysts for promoted water splitting, Acc. Mater. Res. 3 (2022) 449–460, https://doi.org/10.1021/accountsmr.1c00271.

[20] L. Yang, J.X. Yu, Q.Y. Fu, L.L. Kong, X.X. Xu, Mesoporous single-crystalline $SrNbO_2N$: expediting charge transportation to advance solar water splitting, Nano Energy 95 (2022), 107059, https://doi.org/10.1016/J.Nanoen.2022.107059.

[21] L. Yang, J.X. Yu, S.F. Chang, X.X. Xu, Boosting visible-light-driven water splitting over $LaTaON_2$ via Al doping, Sci. China Mater. 65 (2022) 3452–3461, https://doi.org/10.1007/s40843-022-2085-4.

[22] X.X. Xu, R. Wang, X.Q. Sun, M.L. Lv, S. Ni, Layered perovskite compound $NaLaTiO_4$ modified by nitrogen doping as a visible light active photocatalyst for water splitting, ACS Catal. 10 (2020) 9889–9898, https://doi.org/10.1021/acscatal.0c02626.

[23] J.S. Xu, C.S. Pan, T. Takata, K. Domen, Photocatalytic overall water splitting on the perovskite-type transition metal oxynitride $CaTaO_2N$ under visible light irradiation, Chem. Commun. 51 (2015) 7191–7194, https://doi.org/10.1039/c5cc01728a.

[24] S.F. Chang, J.X. Yu, R. Wang, Q.Y. Fu, X.X. Xu, $LaTaON_2$ mesoporous single crystals for efficient photocatalytic water oxidation and Z-scheme overall water splitting, ACS Nano 15 (2021) 18153–18162, https://doi.org/10.1021/acsnano.1c06871.

[25] M.L. Lv, X.Q. Sun, S.H. Wei, C. Shen, Y.L. Mi, X.X. Xu, Ultrathin lanthanum tantalate perovskite nanosheets modified by nitrogen doping for efficient photocatalytic water splitting, ACS Nano 11 (2017) 11441–11448. DOI: 10.1021/acsnano.7b06131.

[26] H. Zou, Y.F. Bao, S.W. Du, X.S. Xin, Y. Qi, G.S. Shao, F.X. Zhang, Visible-light-responsive photocatalyst based on nitrogen-doped bulk oxide $YTaO_{4-x}N_y$ for Z-scheme overall water splitting, Chem. -Asian J. (2023), https://doi.org/10.1002/asia.202300145.

[27] Y.F. Bao, F.X. Zhang, Electronic engineering of ABO_3 perovskite metal oxides based on d^0 electronic-configuration metallic ions toward photocatalytic water splitting under visible light, Small Struct. 3 (2022), 2100226, https://doi.org/10.1002/Sstr.202100226.

[28] F.X. Zhang, A. Yamakata, K. Maeda, Y. Moriya, T. Takata, J. Kubota, K. Teshima, S. Oishi, K. Domen, Cobalt-modified porous single-crystalline $LaTiO_2N$ for highly efficient water oxidation under visible light, J. Am. Chem. Soc. 134 (2012) 8348–8351, https://doi.org/10.1021/ja301726c.

[29] A. Kasahara, K. Nukumizu, T. Takata, J.N. Kondo, M. Hara, H. Kobayashi, K. Domen, $LaTiO_2N$ as a visible-light (<= 600 nm)-driven photocatalyst (2), J. Phys. Chem. B 107 (2003) 791–797, https://doi.org/10.1021/jp026767q.

[30] F.Q. Xiong, L.P. Wan, Y. Li, T. Thomas, F.J. DiSalvo, M.H. Yang, Crucial role of donor density in the performance of oxynitride perovskite $LaTiO_2N$ for photocatalytic water oxidation, ChemSusChem 10 (2017) 930–937, https://doi.org/10.1002/cssc.201601602.

[31] G.A. Lin, X.X. Xu, Ba-modified $LaTiO_2N$ as an efficient visible light active photocatalyst for water oxidation, ACS Sustain. Chem. Eng. 8 (2020) 9641–9649, https://doi.org/10.1021/acssuschemeng.0c00302.

[32] S.G. Ebbinghaus, H.P. Abicht, R. Dronskowski, T. Muller, A. Reller, A. Weidenkaff, Perovskite-related oxynitrides - recent developments in synthesis, characterisation and investigations of physical properties, Prog. Solid State Chem. 37 (2009) 173–205, https://doi.org/10.1016/j.progsolidstchem.2009.11.003.

[33] C. Lawley, A. Arab, A. Hartl, A. Staykov, M. Doebeli, T. Schmitt, D. Pergolesi, T. Lippert, V.N. Strocov, Momentum-resolved electronic structure of $LaTiO_2N$ photocatalysts by resonant Soft-X-ray ARPES, Commun. Mater. 4 (2023) 15, https://doi.org/10.1038/S43246-023-00344-9.

[34] S. Pokrant, M.C. Cheynet, S. Irsen, A.E. Maegli, R. Erni, Mesoporosity in photocatalytically active oxynitride single crystals, J. Phys. Chem. C. 118 (2014) 20940–20947, https://doi.org/10.1021/jp506597h.

[35] C. Lawley, M. Nachtegaal, J. Stahn, V. Roddatis, M. Dobeli, T.J. Schmidt, D. Pergolesi, T. Lippert, Examining the surface evolution of $LaTiO_xN_y$ an oxynitride solar water splitting photocatalyst, Nat. Commun. 11 (2020) 1728, https://doi.org/10.1038/S41467-020-15519-Y.

[36] Y.F. Bao, H. Zou, S.W. Du, X.S. Xin, S.W. Wang, G.S. Shao, F.X. Zhang, Metallic powder promotes nitridation kinetics for facile synthesis of (oxy)nitride photocatalysts, Adv. Mater. (2023), e2302276. DOI:10.1002/adma.202302276.

[37] A. Yamakata, M. Kawaguchi, N. Nishimura, T. Minegishi, J. Kubota, K. Domen, Behavior and energy states of photogenerated charge carriers on Pt- or CoO_x-Loaded $LaTiO_2N$ photocatalysts: time-resolved visible to mid-infrared absorption study, J. Phys. Chem. C. 118 (2014) 23897–23906, https://doi.org/10.1021/jp508233z.

[38] X.W. Lu, A. Bandara, M. Katayama, A. Yamakata, J. Kubota, K. Domen, Infrared spectroscopic study of the potential change at cocatalyst particles on oxynitride photocatalysts for water splitting by visible light irradiation, J. Phys. Chem. C. 115 (2011) 23902–23907, https://doi.org/10.1021/jp207484q.

[39] H.B. Michaelson, The work function of the elements and its periodicity, J. Appl. Phys. 48 (1977) 4729–4733, https://doi.org/10.1063/1.323539.

[40] G.N. Derry, M.E. Kern, E.H. Worth, Recommended values of clean metal surface work functions, J. Vac. Sci. Technol. A 33 (2015), 060801, https://doi.org/10.1116/1.4934685.

[41] D.V. Geppert, A.M. Cowley, B.V. Dore, Correlation of metal-semiconductor barrier height and metal work function; effects of surface states, J. Appl. Phys. 37 (1966) 2458–2467, https://doi.org/10.1063/1.1708837.

[42] Q. Wang, M. Nakabayashi, T. Hisatomi, S. Sun, S. Akiyama, Z. Wang, Z.H. Pan, X. Xiao, T. Watanabe, T. Yamada, N. Shibata, T. Takata, K. Domen, Oxysulfide photocatalyst for visible-light-driven overall water splitting, Nat. Mater. 18 (2019) 827–832, https://doi.org/10.1038/s41563-019-0399-z.

[43] Q.B. Zhu, Y.M. Xuan, K. Zhang, K. Chang, Enhancing photocatalytic CO_2 reduction performance of g-C_3N_4-based catalysts with non-noble plasmonic nanoparticles, Appl. Catal. B-Environ. 297 (2021), 120440, https://doi.org/10.1016/J.Apcatb.2021.120440.

[44] S.L. Shinde, S. Ishii, T.D. Dao, R.P. Sugavaneshwar, T. Takei, K.K. Nanda, T. Nagao, Enhanced solar light absorption and photoelectrochemical conversion using TiN

nanoparticle-incorporated C_3N_4-C dot sheets, ACS Appl. Mater. Interfaces 10 (2018) 2460–2468, https://doi.org/10.1021/acsami.7b15066.
[45] M.J. Zhang, L. Tang, A. Duan, Y. Zhang, F.J. Xiao, Y. Zhu, J.J. Wang, C.Y. Feng, N. Yin, Adjusting charge kinetics of conjugated polymers via integration of LSPR effect with homojunction, Chem. Eng. J. 452 (2023), 139068, https://doi.org/10.1016/J.Cej.2022.139068.
[46] S.F. Chen, Y.G. Yang, W. Liu, Preparation, characterization and activity evaluation of TiN/F-TiO_2 photocatalyst, J. Hazard. Mater. 186 (2011) 1560–1567, https://doi.org/10.1016/j.jhazmat.2010.12.046.
[47] M. Kaur, S.L. Shinde, S. Ishii, W. Jevasuwan, N. Fukata, M.W. Yu, Y.X. Li, J.H. Ye, T. Nagao, Marimo-bead-supported core-shell nanocomposites of titanium nitride and chromium-doped titanium dioxide as a highly efficient water-floatable green photocatalyst, ACS Appl. Mater. Inter 12 (2020) 31327–31339, https://doi.org/10.1021/acsami.0c03781.
[48] M. Hojamberdiev, J.M. Mora-Hernandez, R. Vargas, E.M. Heppke, K. Yubuta, A. Yamakata, Z. Kadirova, L. Torres-Martinez, K. Teshima, M. Lerch, Eliciting the contribution of TiN to photoelectrochemical performance enhancement of Imma-$LaTiO_2N$ at neutral pH, Mater. Today Energy 27 (2022), 101053, https://doi.org/10.1016/J.Mtener.2022.101053.
[49] A. Naldoni, U. Guler, Z.X. Wang, M. Marelli, F. Malara, X.G. Meng, L.V. Besteiro, A. O. Govorov, A.V. Kildishev, A. Boltasseva, V.M. Shalaev, Broadband hot-electron collection for solar water splitting with plasmonic titanium nitride, Adv. Opt. Mater. 5 (2017) 1601031, https://doi.org/10.1002/Adom.201601031.
[50] J. Judek, P. Wrobel, P.P. Michalowski, M. Ozga, B. Witkowski, A. Seweryn, M. Struzik, C. Jastrzebski, K. Zberecki, Titanium nitride as a plasmonic material from near-ultraviolet to very-long-wavelength infrared range, Materials 14 (2021) 7095, https://doi.org/10.3390/Ma14227095.
[51] M.J. Yu, C.L. Chang, H.Y. Lan, Z.Y. Chiao, Y.C. Chen, H.W.H. Lee, Y.C. Chang, S. W. Chang, T. Tanaka, V. Tung, H.S. Chou, Y.J. Lu, Plasmon-enhanced solar-driven hydrogen evolution using titanium nitride metasurface broadband absorbers, ACS Photonics 8 (2021) 3125–3132, https://doi.org/10.1021/acsphotonics.1c00927.
[52] F. Fillot, T. Morel, S. Minoret, I. Matko, S. Maitrejean, B. Guillaumot, B. Chenevier, T. Billon, Investigations of titanium nitride as metal gate material, elaborated by metal organic atomic layer deposition using TDMAT and NH_3, Micro Eng. 82 (2005) 248–253, https://doi.org/10.1016/j.mee.2005.07.083.
[53] V. Mansfeldova, M. Zlamalova, H. Tarabkova, P. Janda, M. Vorokhta, L. Piliai, L. Kavan, Work function of TiO_2 (anatase, rutile, and brookite) single crystals: effects of the environment, J. Phys. Chem. C. 125 (2021) 1902–1912, https://doi.org/10.1021/acs.jpcc.0c10519.
[54] C. Le Paven-Thivet, A. Ishikawa, A. Ziani, L. Le Gendre, M. Yoshida, J. Kubota, F. Tessier, K. Doment, Photoelectrochemical properties of crystalline perovskite lanthanum titanium oxynitride films under visible light, J. Phys. Chem. C. 113 (2009) 6156–6162, https://doi.org/10.1021/jp811100r.
[55] Y.K. Gaudy, S. Dilger, S. Landsmann, U. Aschauer, S. Pokrant, S. Haussener, Determination and optimization of material parameters of particle-based $LaTiO_2N$ photoelectrodes, J. Mater. Chem. A 6 (2018), https://doi.org/10.1039/c8ta03649g.
[56] J.X. Yu, X.X. Xu, $LaNbON_2$ mesoporous single crystals with expedited photocarrier separation for efficient visible-light-driven water redox reactions, J. Catal. 413 (2022) 858–869, https://doi.org/10.1016/j.jcat.2022.07.033.
[57] L. Yang, Q.Y. Fu, L.N. Wang, J.X. Yu, X.X. Xu, Liberating photocarriers in mesoporous single-crystalline $SrTaO_2N$ for efficient solar water splitting, Appl. Catal. B-Environ. 304 (2022), 120934, https://doi.org/10.1016/j.apcatb.2021.120934.
[58] A.E. Maegli, S. Pokrant, T. Hisatomi, M. Trottmann, K. Domen, A. Weidenkaff, Enhancement of photocatalytic water oxidation by the morphological control of $LaTiO_2N$ and cobalt oxide catalysts, J. Phys. Chem. C. 118 (2014) 16344–16351, https://doi.org/10.1021/jp4084162.
[59] T. Takashima, T. Sano, H. Irie, Improvement of the photocatalytic water splitting activity of silver tantalate by photodeposited platinum and cobalt-oxide nanoclusters, Electrochemistry 84 (2016) 784–788, https://doi.org/10.5796/electrochemistry.84.784.
[60] L. Huang, X. Liu, H.C. Wu, X.L. Wang, H.M. Wu, R.G. Li, L.Y. Shi, C. Li, Surface state modulation for size-controllable photodeposition of noble metal nanoparticles on semiconductors, J. Mater. Chem. A 8 (2020) 21094–21102, https://doi.org/10.1039/c9ta14181b.
[61] Y. Hiramachi, H. Fujimori, A. Yamakata, Y. Sakata, Achievement of high photocatalytic performance to $BaTi_4O_9$ toward overall H_2O splitting, ChemCatChem 11 (2019) 6213–6217, https://doi.org/10.1002/cctc.201901564.
[62] T. Sano, N. Negishi, K. Uchino, J. Tanaka, S. Matsuzawa, K. Takeuchi, Photocatalytic degradation of gaseous acetaldehyde on TiO_2 with photodeposited metals and metal oxides, J. Photoch. Photobio. A 160 (2003) 93–98, https://doi.org/10.1016/S1010-6030(03)00226-0.
[63] S.F. Chang, L. Shi, J.X. Yu, R. Wang, X.X. Xu, G. Liu, Boosted Z-scheme photocatalytic overall water splitting with faceted Bi_4TaO_8Cl crystals as water oxidation photocatalyst, Appl. Catal. B-Environ. 328 (2023), 122541, https://doi.org/10.1016/j.apcatb.2023.122541.
[64] J.X. Yu, S.F. Chang, L. Shi, X.X. Xu, Single-crystalline Bi_2YO_4Cl with facet-aided photocarrier separation for robust solar water splitting, ACS Catal. 13 (2023) 3854–3863, https://doi.org/10.1021/acscatal.2c05768.
[65] S.H. Wei, S.F. Chang, J. Qian, X.X. Xu, Selective cocatalyst deposition on $ZnTiO_{3-x}N_y$ hollow nanospheres with efficient charge separation for solar-driven overall water splitting, Small 17 (2021), 2100084, https://doi.org/10.1002/Smll.202100084.
[66] N.C. Hyatt, J.A. Hriljac, T.P. Comyn, Cation disorder in $Bi_2Ln_2Ti_3O_{12}$ aurivillius phases (Ln = La, Pr, Nd and Sm), Mater. Res. Bull. 38 (2003) 837–846, https://doi.org/10.1016/S0025-5408(03)00032-1.
[67] Z. Wang, Y. Inoue, T. Hisatomi, R. Ishikawa, Q. Wang, T. Takata, S.S. Chen, N. Shibata, Y. Ikuhara, K. Domen, Overall water splitting by Ta_3N_5 nanorod single crystals grown on the edges of $KTaO_3$ particles, Nat. Catal. 1 (2018) 756–763, https://doi.org/10.1038/s41929-018-0134-1.
[68] Y.W. Zhang, L.L. Kong, E.Y. Konysheva, X.X. Xu, Expediting photocarrier separation in Ta_3N_5@$CaTaO_2N$ heterostructures with seamless interfaces for photocatalytic water oxidation under visible light, Appl. Catal. B-Environ. 317 (2022), 121712, https://doi.org/10.1016/j.apcatb.2022.121712.
[69] G.A. Lin, C. Zhang, X.X. Xu, Ta_3N_5-$LaTaON_2$ heterojunction with matched interfaces to accelerate charge separation for efficient photocatalytic water oxidation, J. Mater. Sci. Technol. 154 (2023) 241–250, https://doi.org/10.1016/j.jmst.2022.12.069.
[70] Y.Z. Zhang, J.W. Shi, C. Cheng, S.C. Zong, J.F. Geng, X.J. Guan, L.J. Guo, Hydrothermal growth of $Co_3(OH)_2(HPO_4)_2$ nano-needles on $LaTiO_2N$ for enhanced water oxidation under visible-light irradiation, Appl. Catal. B-Environ. 232 (2018) 268–274, https://doi.org/10.1016/j.apcatb.2018.03.067.
[71] A. Kasahara, K. Nukumizu, G. Hitoki, T. Takata, J.N. Kondo, M. Hara, H. Kobayashi, K. Domen, Photoreactions on $LaTiO_2N$ under visible light irradiation, J. Phys. Chem. A 106 (2002) 6750–6753, 10.1021/jp025961+.
[72] F.F. Wu, G. Liu, X.X. Xu, Efficient photocatalytic oxygen production over Ca-modified $LaTiO_2N$, J. Catal. 346 (2017) 10–20, https://doi.org/10.1016/j.jcat.2016.11.022.
[73] K. Kawashima, M. Hojamberdiev, H. Wagata, M. Nakayama, K. Yubuta, S. Oishi, K. Domen, K. Teshima, Amount of tungsten dopant influencing the photocatalytic water oxidation activity of $LaTiO_2N$ crystals grown directly by an NH_3-assisted flux method, Catal. Sci. Technol. 6 (2016) 5389–5396, https://doi.org/10.1039/c5cy02046h.
[74] M. Matsukawa, R. Ishikawa, T. Hisatomi, Y. Moriya, N. Shibata, J. Kubota, Y. Ikuhara, K. Domen, Enhancing photocatalytic activity of $LaTiO_2N$ by removal of surface reconstruction layer, Nano Lett. 14 (2014) 1038–1041, https://doi.org/10.1021/nl404688h.
[75] S.K. Kuk, Y. Ham, K. Gopinath, P. Boonmongkolras, Y. Lee, Y.W. Lee, S. Kondaveeti, C.G. Ahn, B. Shin, J.K. Lee, S. Jeon, C.B. Park, Continuous 3D titanium nitride nanoshell structure for solar-driven unbiased biocatalytic CO_2 reduction, Adv. Energy Mater. 9 (2019) 1900029, https://doi.org/10.1002/Aenm.201900029.
[76] R.G. Li, F.X. Zhang, D.G. Wang, J.X. Yang, M.R. Li, J. Zhu, X. Zhou, H.X. Han, C. Li, Spatial separation of photogenerated electrons and holes among {010} and {110} crystal facets of $BiVO_4$, Nat. Commun. 4 (2013) 1432, https://doi.org/10.1038/Ncomms2401.